



Schottky barrier tuning via surface plasmon and vacancies for enhanced photocatalytic H₂ evolution in seawater

Chuchu Cheng, Jingwen Zhang, Renyou Zeng, Fangshu Xing, Caijin Huang^{*}

State Key Laboratory of Photocatalysis on Energy and Environment, College of Chemistry, Fuzhou University, Fuzhou 350116, PR China

ARTICLE INFO

Keywords:

Photocatalysis
Surface plasmon resonance
Sulfur vacancy
Schottky barrier
Seawater

ABSTRACT

Although Schottky barriers at the interface of metal/semiconductor help electron/hole separation in photocatalysis, they also limit the migration of electrons across the interface. Herein, we tune Schottky barriers over Ni/S vacancy-rich Mn_{0.3}Cd_{0.7}S (Ni/MCS-s) composites prepared by self-assembly and photochemical method. The Ni/MCS-s heterostructures exhibits superior hydrogen production activity up to 164.1 mmol/h/g in simulated seawater (3.5 wt% NaCl), which is 68 and 5 times higher than MCS-s and 1 wt% Pt/MCS-s, respectively. The apparent quantum yield reached 60.4% at 420 nm. The excellent photocatalytic performance of Ni/MCS-s results from the coupling of plasmonic Ni and S vacancies, which can effectively lower Schottky barrier and enhance hot electrons across the interface for photocatalytic process. Moreover, the Ni layer effectively prevents the catalyst from being corroded in seawater. This work provides a feasible strategy for designing efficient photocatalysts for solar energy conversion in seawater.

1. Introduction

Photocatalytic hydrogen production from water addresses clean energy conversion by exploiting green, sustainable solar power [1]. Up to now, most of the researches for photocatalytic hydrogen evolution were conducted in deionized water or freshwater system [2]. Notably, only about 1% of the water on Earth is fresh water and more than 97% of the earth's water is salty [3]. The growing population and rapidly increasing industry aggravated the freshwater shortage. Thus, using seawater and readily available solar energy to obtain renewable hydrogen is a worthy proposition. Many reports have demonstrated that the abundant ions in seawater can significantly affect photocatalytic performance [4]. The natural seawater contains an average salinity of ~3.5%, in which NaCl is the predominant species [5]. Na⁺ ions could help TiO₂ to absorb sacrificial agent (ethanol) under basic or neutral conditions, which is beneficial to hydrogen-evolution process [6]. Other cations (e.g., K⁺, Mg²⁺ and Ca²⁺) could promote the electron sink effect of carbon dots and thus improve the photocatalytic activity [7]. However, Ho et al. proposed that the competition between Cl⁻ and the reactant for the active sites suppress the adsorption of H⁺ or the sacrificial agent [8]. Moreover, due to the high salinity of natural seawater, the dissolved salts may deactivate catalysts or consume the photo-induced carriers [9], resulting in lower activity for photocatalysts

(e.g., CuO/nano TiO₂ [10], CoP/Cd₃Zn_{1-x}Se [11]) in seawater than in pure water. In light of this, the development of highly efficient and salt corrosion-resistant photocatalysts for hydrogen production in seawater is highly desirable.

Some anti-corrosion efforts have been made for photocatalysis in seawater, such as co-catalyst modification (e.g., oxides, sulfide and metal) [12]. It is well-known that Ni has been used to improve steel corrosion resistance in marine environment [13], and acts as an effective co-catalyst for solar-driven hydrogen production [14,15]. Hence, it is interesting to use Ni as photo-cocatalyst for seawater H₂ production. Additionally, Nickel, a kind of non-noble plasmonic metal [16], exhibits strong light absorption and can provide abundant hot electrons for the photocatalytic process under light irradiation. The plasmonic Ni/TiO₂ heterostructure showed tunable visible light absorption and significantly promoted the degradation of methylene blue (MB) [17]. The hierarchical TaON@plasmonic Ni hybrid exhibited enhanced photocatalytic activity of CO₂ reduction through the coupling of Schottky junction and plasmonic hot carrier injection [18].

The integration of plasmonic metals with semiconductors is an attractive topic in the field of photocatalysis due to the strong light absorption and fast plasmonic energy transfer of the localized surface plasmon resonance (LSPR) [19]. The highly energetic hot electrons induced by LSPR are directly injected into the conduction band (CB) of

^{*} Corresponding author.

E-mail address: cjhuang@fzu.edu.cn (C. Huang).

<https://doi.org/10.1016/j.apcatb.2022.121321>

Received 24 January 2022; Received in revised form 10 March 2022; Accepted 13 March 2022

Available online 19 March 2022

0926-3373/© 2022 Elsevier B.V. All rights reserved.

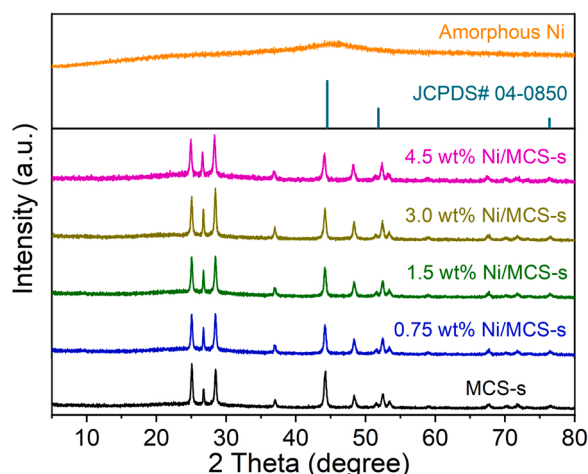


Fig. 1. XRD patterns of Ni, MCS-s and Ni/MCS-s nanocomposites.

n-type semiconductors, and thus induce reductive half-reactions [20]. The plasmonic metal not only improves the photoabsorption via LSPR but also provides a Schottky barrier at the metal/semiconductor interface. The Schottky barrier can inhibit the recombination of photo-induced electrons and holes [21], which is beneficial to the photocatalytic process. However, Schottky barrier has high contact resistance and limits the free flow of carriers across the interface for photocatalysis [22]. For plasmonic metal-semiconductor system, the kinetic energy of the hot electrons must be greater than the Schottky barrier height (SBH) to ensure the happen of the hot-electron-injection process [23]. As a result, some hot electrons cannot cross the Schottky barrier and get lost in the metal via recombination with the holes, which reduces the efficiency of plasmonic photocatalysts [24]. Therefore, the SBH is also an important parameter for the plasmon-induced photocatalysis, which can be estimated by subtracting the electron affinity (χ) of the semiconductor from the work function of the plasmonic metal (W_{FM}) [25]. Adjusting SBH is a feasible route to smooth the plasmon-driven hot-electron transfer over the metal/semiconductor interface. Under photoexcitation, a fraction of hot electrons in plasmonic metals would distribute above the Fermi level due to the plasma oscillation [26], which can lower the effective work function and decrease SBH [27].

The band structure at the interface can be changed when there are vacancies or foreign atoms in the semiconductor [28]. The anion vacancy (e.g., O vacancy, S vacancy) could produce positively charged centers on the surface [29], form surface states in the bandgap of the semiconductor, and affect the interfacial charge and space-charge region [30]. This can decrease the CB of semiconductors around the interface, tune the Schottky barrier, and thus facilitate the transboundary movement of electrons [31]. Particularly, S vacancy engineering is an important strategy to notably increase the density of active sites and introduce the surface states in the band structure [32], which is beneficial to the hydrogen production process. Furthermore, positively charged S vacancies can act as electron traps and improve electron-hole separation efficiency [33]. For example, S vacancy-rich $Mn_{0.3}Cd_{0.7}S$ (MCS-s) prepared by excess thioacetamide (TAA), has more than 3 times photocatalytic H_2 production rate than S vacancy-poor $Mn_{0.3}Cd_{0.7}S$ (MCS-p) [34,35].

Herein, we designed plasmonic Ni/S vacancy-rich $Mn_{0.3}Cd_{0.7}S$ (Ni/MCS-s) nanorods via a simple photo-induced deposition method (Fig. S1). The hydrogen production performance of the as-obtained Ni/MCS-s samples was remarkably promoted and reached 164.1 mmol/h/g in simulated seawater (3.5 wt% NaCl), which is better than that in water (121.5 mmol/h/g), 68 times higher than that of pure MCS-s, and approximately 5 times higher than that of 1 wt% Pt/ $Mn_{0.3}Cd_{0.7}S$. The optimal Ni/MCS-s composite achieved an AQY value of 60.4% in 3.5 wt

% NaCl at 420 nm, which is remarkably superior to previous reports on photocatalytic seawater splitting. In addition, we investigated the effect of S vacancy, different salts and salt concentrations on photocatalytic hydrogen performance. Furthermore, combined with photocatalytic activity and some characterizations such as UV-vis diffuse reflectance spectroscopy (DRS), electron paramagnetic resonance (EPR), X-ray photoelectron spectroscopy (XPS) and electrochemical measurements, the synergistic effect of S vacancies and plasmonic Ni were investigated. Meanwhile, a possible photocatalytic reaction mechanism for Ni/MCS-s composites will be discussed.

2. Experimental section

2.1. Synthesis of $Mn_{0.3}Cd_{0.7}S$ nanorods

S vacancy-rich $Mn_{0.3}Cd_{0.7}S$ (MCS-s) nanorods were obtained by a solvothermal method based on a previous report [35]. Typically, 6 mmol $Mn(OAc)_2 \cdot 4 H_2O$, 14 mmol $Cd(OAc)_2 \cdot 2 H_2O$ and excess thioacetamide (TAA, 25 mmol) were dissolved in a mixture of water (30 mL) and ethylenediamine (30 mL) and kept stirring for 30 min. Then, the above suspension was transferred into a 100 mL Teflon-lined stainless steel autoclave and heated at 200 °C for 24 h. After cooling to room temperature, the precipitate was collected, washed with water and ethanol, and dried at 60 °C under vacuum overnight. In addition, S vacancy-poor $Mn_{0.3}Cd_{0.7}S$ (MCS-p) nanorods were synthesized similarly by the above procedure except adding stoichiometric TAA amount (20 mmol).

2.2. Synthesis of Ni/ $Mn_{0.3}Cd_{0.7}S$ composites

The Ni/S vacancy-rich $Mn_{0.3}Cd_{0.7}S$ (Ni/MCS-s) were synthesized via a photo-induced deposition method [36]. Firstly, 50 mg as-prepared MCS-s was dispersed in 80 mL ethanol solution. Then, A certain volume of 0.1 M $Ni(NO_3)_2$ was added to the above solution. The system was evacuated with N_2 for 20 min to empty oxygen and then illuminated by a 300 W Xe lamp with a 420 nm cut-off filter for 10 min. The resultant green product was obtained after centrifugal separation, washed with water and ethanol, and dried under vacuum at 60 °C overnight. Besides, Ni/S vacancy-poor $Mn_{0.3}Cd_{0.7}S$ (Ni/MCS-p) was prepared by the same procedure using MCS-p instead of MCS-s.

2.3. Synthesis of control experiment samples

The 1 wt% Pt/S vacancy-rich $Mn_{0.3}Cd_{0.7}S$ (Pt/MCS-s) were synthesized via the photo-deposition method as reported [37]. Briefly, 50 mg MCS-s and 133 μ L 10 g/L $H_2PtCl_6 \cdot 6 H_2O$ were dispersed in 80 mL aqueous methanol solution (10 vol%) and magnetically stirred for 10 min. The reactor was evacuated with N_2 for 20 min to empty air, and then a 300 W Xenon lamp was used to illuminate the suspension for 30 min. The product was obtained after centrifugal separation, washed with water and ethanol, and dried under vacuum at 60 °C overnight.

1.5 wt% NiO/MCS-s was obtained by oxidizing 1.5 wt% Ni/MCS-s in air at 60 °C overnight. 1.5 wt% NiS/MCS-s was prepared under a condition similar to 1.5 wt% Ni/MCS-s except for adding Na_2SO_3 before photo-deposition. 15 mol% $Ni(OH)_2$ /MCS-s was synthesized via a coprecipitation method as reported [35].

2.4. Synthesis of amorphous Ni

Amorphous Ni was synthesized by a liquid-phase reduction process, in which $Ni(NO_3)_2 \cdot 6 H_2O$ and $NaBH_4$ as the reactant [38]. 2.5 g $Ni(NO_3)_2 \cdot 6 H_2O$ was dissolved in 50 mL ethanol in a three-neck flask with vigorous stirring, and pure N_2 was bubbled through the solution for 30 min to remove oxygen. Next, 75 mL water containing 2.0 g $NaBH_4$ was added into the above solution under intense stirring and N_2 flow. After the reaction was processed for 30 min, the obtained amorphous Ni was filtered, washed with water and ethanol, and dried at 60 °C under

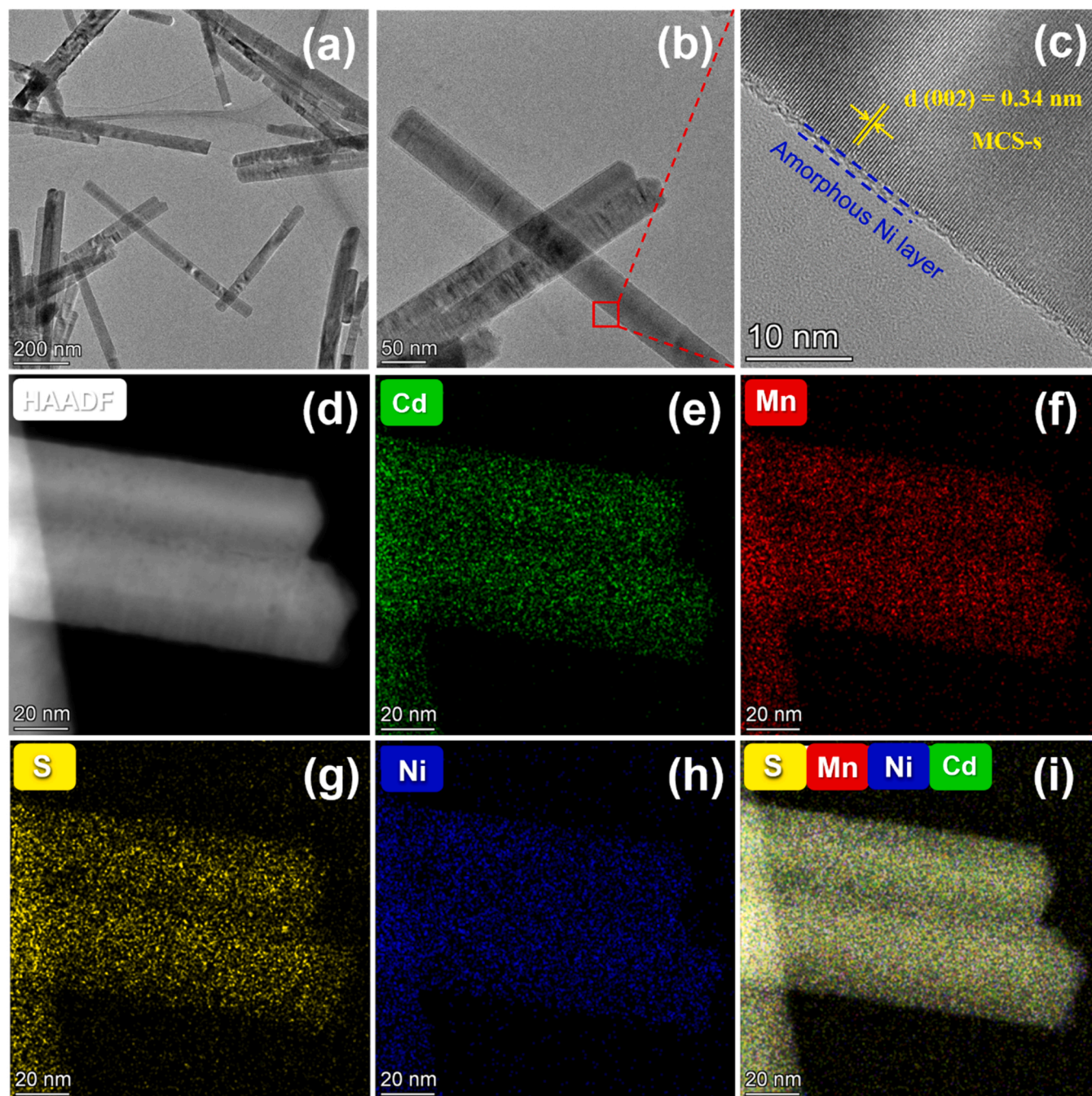


Fig. 2. Electron microscopy images of 1.5 wt% Ni/MCS-s: (a,b) TEM, (c) HRTEM, (d) HAADF-STEM and (e-i) EDX mapping.

vacuum overnight.

2.5. Electrochemical and photoelectrochemical measurements

Photoelectrochemical measurements were performed on a typical electrochemical workstation (SAS SP-300, Bio-Logic) by using a conventional three-electrode cell. Ag/AgCl/sat. KCl electrodes and Pt wires were used as the reference electrode and counter electrode, respectively. The as-prepared samples coated on FTO glass acted as the working electrode [39]. Linear sweep voltammetry (LSV) spectra and Mott-Schottky plots were obtained in the electrolyte of 0.2 mol/L Na_2SO_4 , while electrochemical impedance spectra (EIS) and photocurrent response experiments were conducted in a solution of sacrificial agents (0.35 M Na_2S and 0.25 M Na_2SO_3). A Xe lamp (300 W,

PLS-SXE300) with a 420 nm cut-off filter was utilized as a visible light source for the photocurrent response experiment.

2.6. Photocatalytic activity tests

In a typical process, the photocatalyst (5 mg) was added into a solution of sacrificial reagent (50 mL, 0.35 M Na_2S and 0.25 M Na_2SO_3) in a 500 mL quartz photoreactor. Before irradiation, the reactor was degassed for 15 min and kept at 5 °C through a recirculating cooling water system. Then the solution was irradiated with a 300 W xenon lamp (PLS-SXE 300, PerfectLight) fitted with a 420 nm cut-off filter. Gas chromatography was used to detect the H_2 evolved during photocatalysis with a TCD detector. The value of AQY was measured according to the following formula:

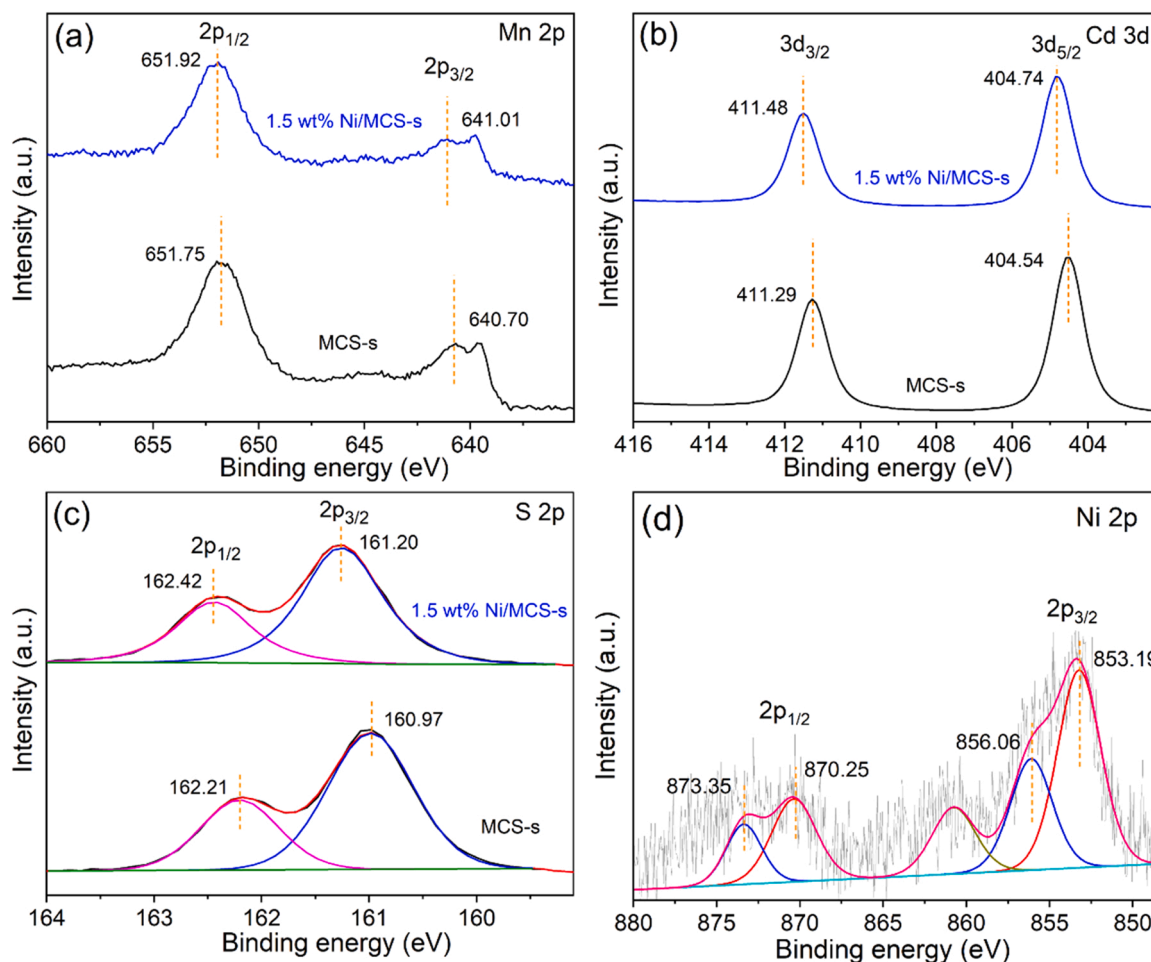


Fig. 3. XPS high-resolved spectra of 1.5 wt% Ni/MCS-s and MCS-s samples: (a) Mn 2p, (b) Cd 3d and (c) S 2p (d) Ni 2p.

$$\text{AQY (\%)} = \frac{2 \times \text{number of evolved H}_2 \text{ molecules}}{\text{number of incident photons}} \times 100$$

3. Results and discussion

3.1. Morphology and chemical structure characterization

Ni/S vacancy-rich $\text{Mn}_{0.3}\text{Cd}_{0.7}\text{S}$ (Ni/MCS-s) composites were prepared by a facile photo-induced synthesis route (Fig. S1). The added Ni^{2+} ions can be uniformly attached to the surface of MCS-s nanorods through electrostatic attraction (Fig. S2), and an ultrathin Ni layer was in-situ generated under light irradiation. From the XRD patterns of the samples (Fig. 1), the diffraction peaks at 25.03° , 28.44° , 36.96° and 44.16° are assigned to the solid solution $\text{Mn}_{0.3}\text{Cd}_{0.7}\text{S}$ [35]. No obvious peaks for the Ni layer can be found in the Ni/MCS-s composites, indicating that the nickel layer is amorphous due to the mild condition synthesis. In addition, the big hump between 38° and 55° is attributed to the scattered X-rays from amorphous Ni [38].

The morphological characterization was observed by TEM, SEM, and high-resolution TEM (HRTEM). MCS-s shows a smooth nanorod structure, and no obvious change in morphology after Ni loading (Fig. 2a and Fig. S3). The length and diameter of the nanorods are approximately $0.5\text{--}2.0\ \mu\text{m}$ and $40\text{--}50\ \text{nm}$, respectively. Besides, the HRTEM image (Fig. 2c) exhibits a lattice spacing of $0.34\ \text{nm}$ corresponding to the (002) lattice plane of MCS-s, and an ultrathin amorphous Ni layer ($1\text{--}2\ \text{nm}$) grown on the MCS-s surface. The HAADF-STEM and EDX elemental mapping images (Fig. 2d-i) reveal that Cd, Mn, S and Ni are uniformly distributed over the whole nanorod, illustrating the covering of

amorphous Ni layer. The real Ni mass fraction of 1.5 wt% Ni/MCS-s is $0.42\ \text{wt\%}$ (Table S1).

The existence of S vacancies in the samples was confirmed by EPR spectra (Fig. S4). The sharp ESR signal at $3518\ \text{G}$ (g -value of 2.003) originates from the single electrons trapped by S vacancies [35]. The EPR signal intensity of MCS-p is lower than that of MCS-s due to the formation of S vacancy which is mainly caused by excess TAA molecules in the preparation process [35]. After Ni loading, 1.5 wt% Ni/MCS-s and 1.5 wt% Ni/MCS-p exhibit stronger EPR signals than MCS-s and MCS-p, respectively, due to the superparamagnetism of metallic Ni with a size small enough [40,41]. The highest intensity of EPR signals for 1.5 wt% Ni/MCS-s is owing to the overlapping of the EPR signals from Ni and S vacancies [42].

The composition and chemical state of samples were determined by XPS. The XPS survey spectrum (Fig. S5) displays the existence of Cd, Mn, S and Ni elements, which confirms the successful loading of Ni on MCS-s. As for 1.5 wt% Ni/MCS-s, the Mn 2p spectrum (Fig. 3a) presents two peaks at $651.92\ \text{eV}$ and $641.01\ \text{eV}$, belonging to the $2p_{1/2}$ and $2p_{3/2}$ of Mn^{2+} , respectively. The peaks located at $411.48\ \text{eV}$ and $404.74\ \text{eV}$ correspond to the $3d_{3/2}$ and $3d_{5/2}$ of Cd^{2+} (Fig. 3b) [43]. In the S 2p spectrum (Fig. 3c), two peaks at $162.42\ \text{eV}$ and $161.20\ \text{eV}$ could be assigned to the $2p_{1/2}$ and $2p_{3/2}$ of S^{2-} , respectively. Compared with MCS-s, the binding energy of Cd, Mn and S of 1.5 wt% Ni/MCS-s appears a positive shift, manifesting that a portion of electrons are transferred from MCS-s to Ni. When MCS-s is in contact with metallic Ni with a lower Fermi level, electrons will flow from MCS-s to Ni until they reach an equilibrium Fermi energy, and the band structure of MCS-s at the Ni/MCS-s interface is deformed to construct a Schottky barrier. In the Ni 2p spectra of

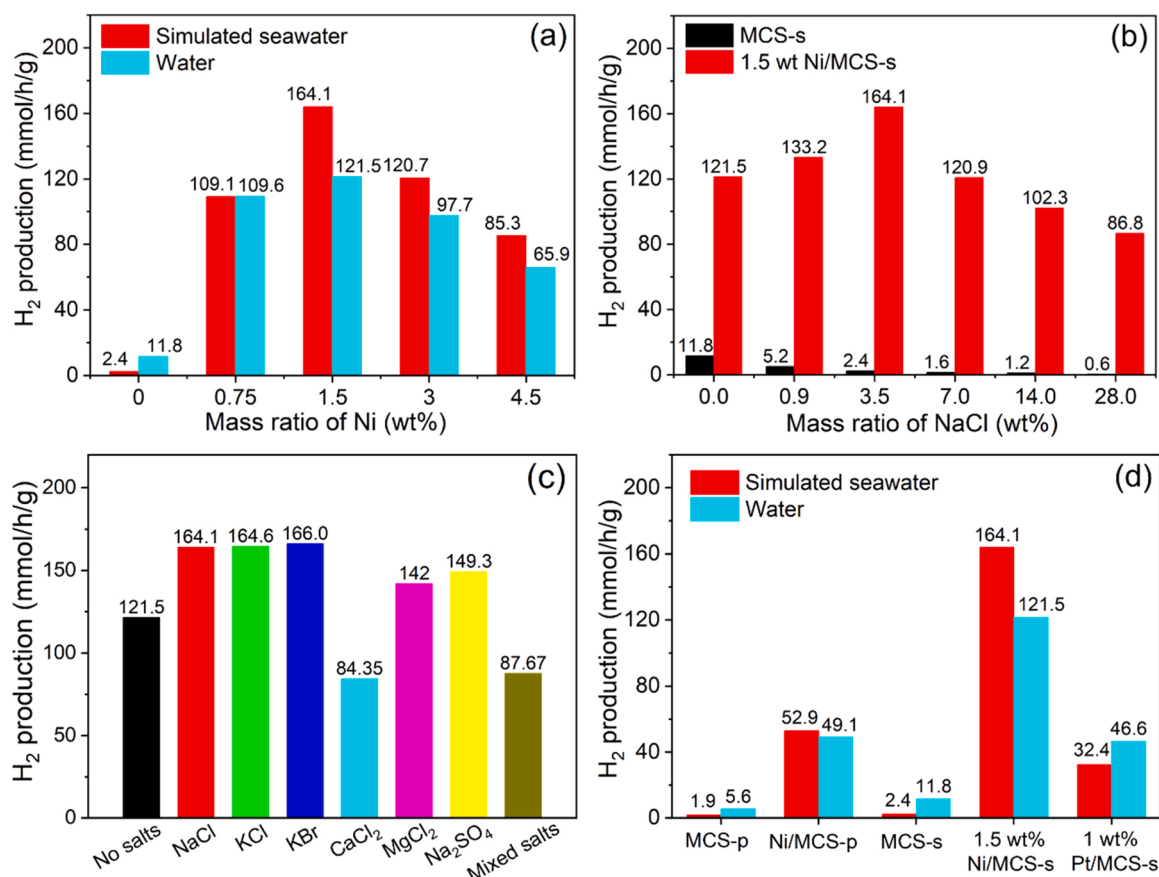


Fig. 4. (a) Photocatalytic H₂ production of Ni/MCS-s with different Ni contents in water and simulated seawater (3.5 wt% NaCl). (b) H₂-production rate of 1.5 wt% Ni/MCS-s and MCS-s at a given NaCl concentration gradient (0–28 wt%). (c) H₂-evolution rate of 1.5 wt% Ni/MCS-s in the presence of other salts. (All salts with a positive and negative charge equal to that of 3.5 wt% NaCl, details are displayed in Table S2; The mixed salts simulate natural seawater, details are listed in Table S3). (d) Photocatalytic performance of samples in water and simulated seawater. Reaction conditions: 5 mg photocatalyst, visible light irradiation ($\lambda > 420$ nm), 5 °C, and 0.35 M Na₂S/0.25 M Na₂SO₃ as sacrificial agent.

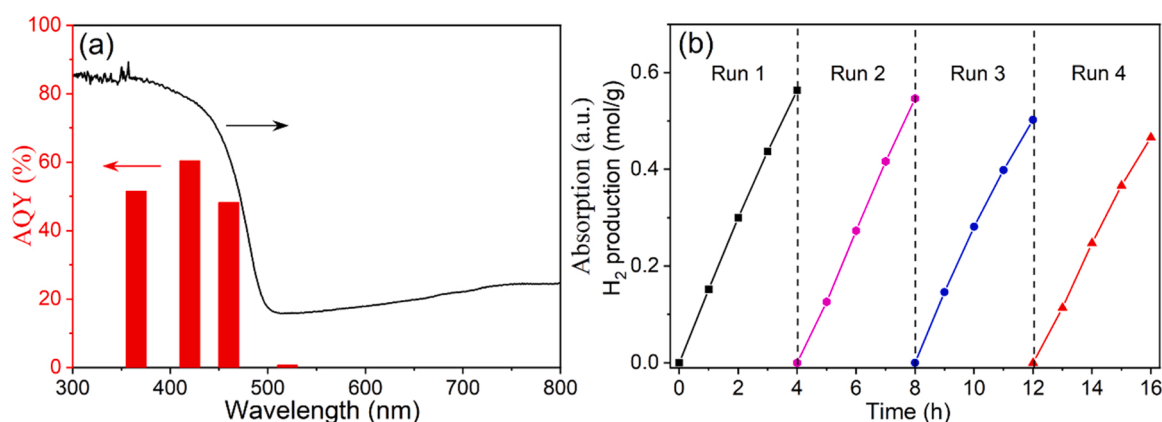


Fig. 5. (a) AQY values of 1.5 wt% Ni/MCS-s at specific wavelengths (365, 420, 460 and 520 nm) in 3.5 wt% NaCl and its UV-vis spectrum. (b) Cycling test of 1.5 wt% Ni/MCS-s in simulated seawater.

Ni/MCS-s (Fig. 3d), the peaks at 870.25 and 853.19 eV could be attributed to Ni⁰, while those at 873.35 and 856.06 eV could be assigned to Ni²⁺ [39]. The presence of Ni²⁺ is most likely attributed to the formation of Ni-O or Ni-S bonds [44].

3.2. Photocatalytic H₂ evolution activity and stability analysis

The photocatalytic H₂ production of the as-prepared samples was

evaluated in water and seawater under visible light ($\lambda \geq 420$ nm). In Fig. 4a, the H₂-production rate of pure MCS-s in simulated seawater (2.4 mmol/h/g) is obviously lower than in water (11.8 mmol/h/g), because many ionic components in seawater strongly affect the intrinsic structure and electron transport of MCS-s [7]. After being loaded with an amorphous Ni layer, the photocatalytic performance of MCS-s is remarkably enhanced. Particularly, the 1.5 wt% Ni/MCS-s composite exhibits the highest photocatalytic activity (164.1 mmol/h/g) in

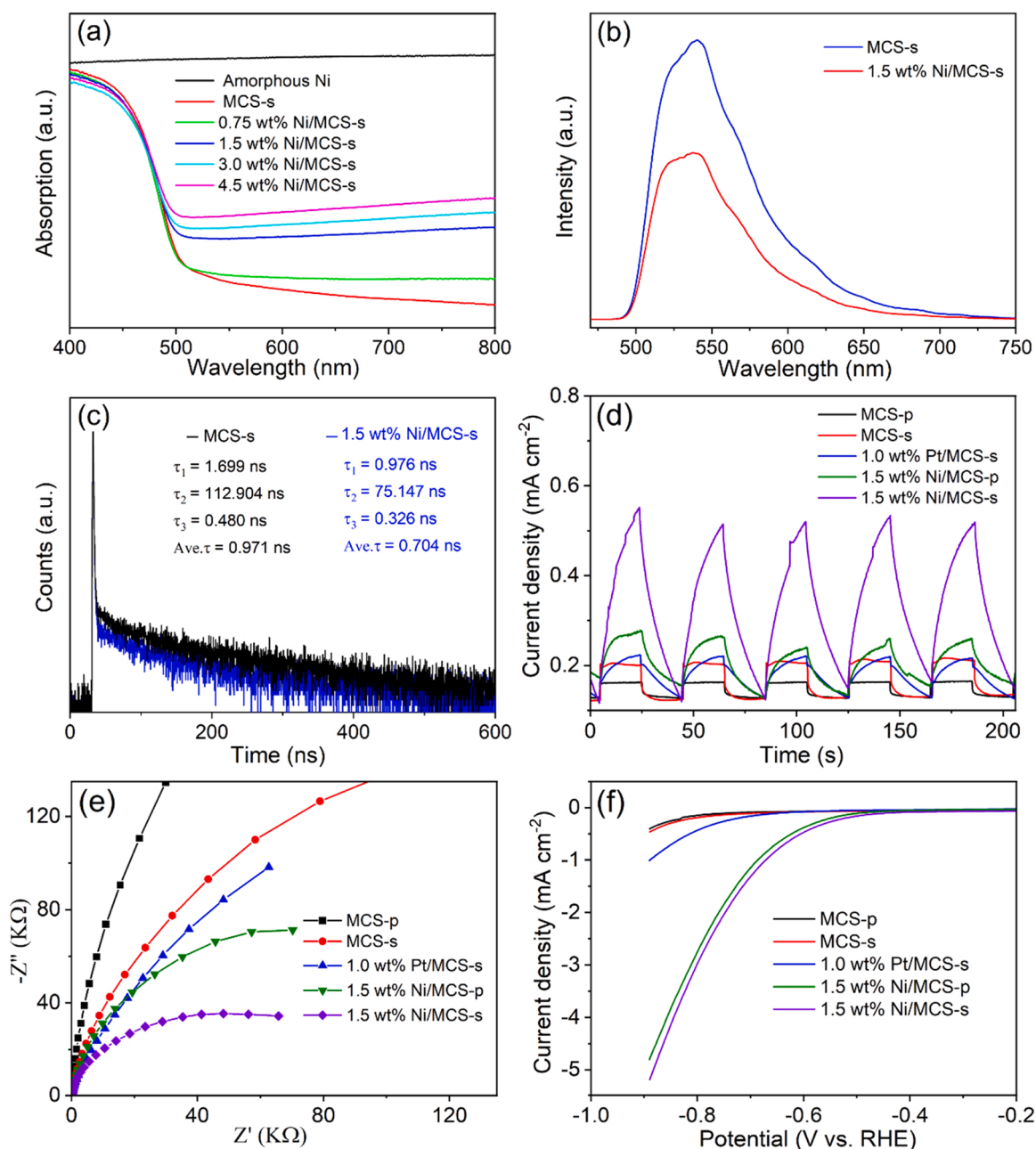


Fig. 6. (a) UV-vis spectra of Ni, MCS-s and Ni/MCS-s composites. (b) PL and (c) TRPL spectra of MCS-s and 1.5 wt% Ni/MCS-s. (d) Transient photocurrent responses, (e) EIS Nyquist plots and (f) LSV polarization curves of MCS-p, MCS-s, 1.0 wt% Pt/ MCS-s, 1.5 wt% Ni/MCS-p and 1.5 wt% Ni/MCS-s.

seawater, which is better than in water (121.5 mmol/h/g) and 68 times higher than that of pure MCS-s. And the H₂-evolution rate of 1.5 wt% Ni/MCS-s reaches 184.5 mmol/g/h at 25 °C (Fig. S6). The presence of the amorphous Ni layer can improve H₂-evolution rate even in salt solutions. To further study the effect of NaCl on hydrogen production, different NaCl concentrations were used for 1.5 wt% Ni/MCS-s and MCS-s (Fig. 4b). 1.5 wt% Ni/MCS-s achieved the optimal photocatalytic activity at 3.5 wt% NaCl which is close to the average NaCl concentration of natural seawater [5]. Since natural seawater contains many kinds of ions (major ions: Na⁺, K⁺, Ca²⁺, Mg²⁺, Cl⁻, Br⁻ and SO₄²⁻) [12], various saline solutions were used to investigate the photocatalytic performance of 1.5 wt% Ni/MCS-s (Fig. 4c). Most of the saline solutions have positive effect on hydrogen production except for Ca²⁺ and Mg²⁺ solutions, because excess alkali earth metal cations produce precipitation with the sacrifice agents S²⁻ and SO₃²⁻. This illustrates that specific anion (e.g., Cl⁻) or cation (e.g., Na⁺) is not the determinant for the

photocatalysis of Ni/MCS-s in seawater, the charges that the ions carry may be the main reason for the enhanced photocatalytic activity. To gain insights into the positive effect of salts, the zeta potential of samples was measured to study the effect of surface charge on ion adsorption (Fig. S7a). The zeta potential of 1.5 wt% Ni/MCS-s reached -7.79 mV, which is more negative than that of MCS-s (-4.42 mV). Besides, with the increase of NaCl concentration (Fig. S7b), the value of zeta potential gradually becomes more negative. This means that more negative charges are accumulated on the surface of 1.5 wt% Ni/MCS-s, which is in favor of adsorbing cations (such as Na⁺, K⁺ and Ca²⁺) in seawater [12]. Furthermore, control experiments for different photocatalysts are shown in Fig. 4d and Fig. S9. MCS-s has better photocatalytic performance than S vacancy-poor Mn_{0.3}Cd_{0.7}S (MCS-p) in both water and simulated seawater, which indicates that S vacancy is of benefit to hydrogen production in both water and seawater. Remarkably, the H₂-evolution rate of 1.5 wt% Ni/MCS-s in seawater is approximately 5

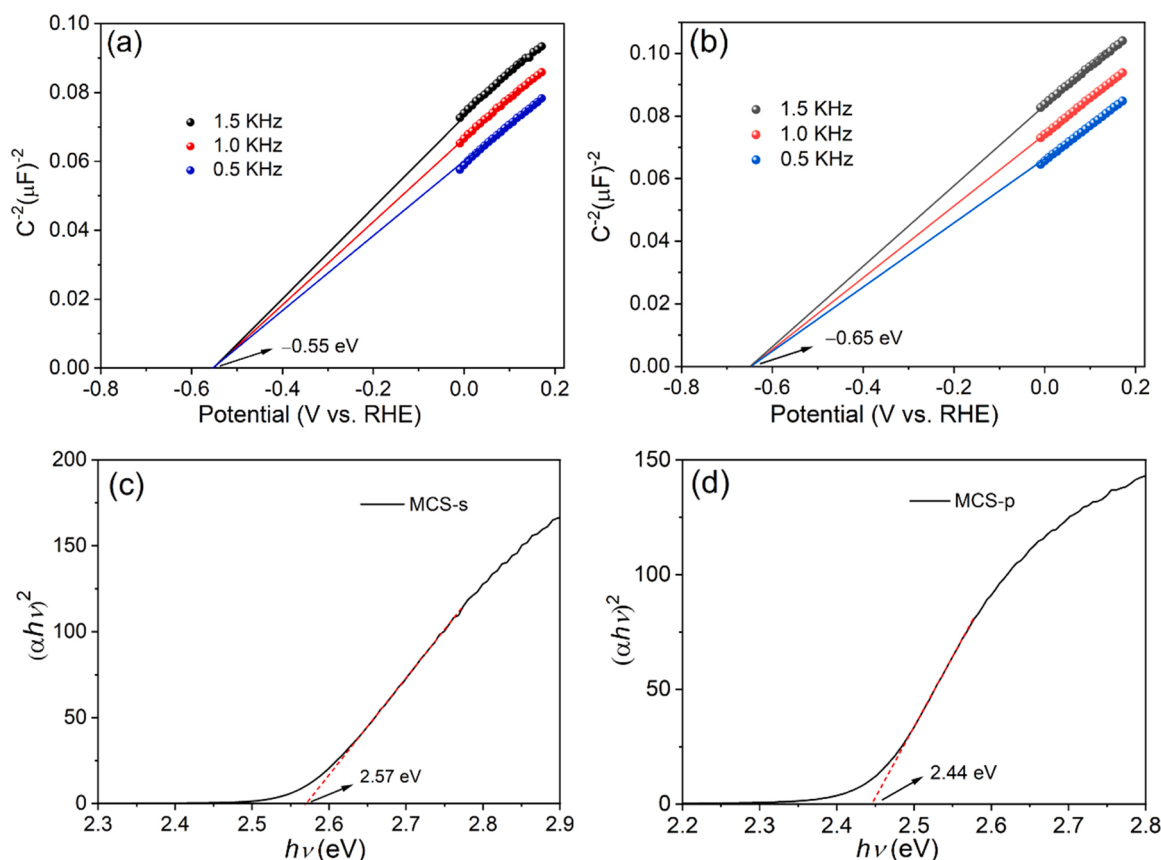


Fig. 7. Mott-Schottky plots of (a) MCS-s and (b) MCS-p; Tauc plots of (c) MCS-s and (d) MCS-p.

times higher than that of 1 wt% Pt/MCS-s and also better than that of other $\text{Mn}_x\text{Cd}_{1-x}\text{S}$ -based photocatalysts (Table S4). After replacing plasmonic Ni on the surface of MCS-s with non-plasmonic materials (NiS, NiO and $\text{Ni}(\text{OH})_2$) (Fig. S9), the photocatalytic performance was significantly decreased, implying that the LSPR effect is of importance for enhancing photocatalytic activity in our system. Besides, we also optimized the photo-reduction deposition time and sample usage for photocatalytic hydrogen production (Fig. S10).

To further confirm the existence of hot electrons of Ni, the hydrogen evolution activity of the samples (Fig. S11a) were measured under near infrared (NIR) ($\lambda > 800$ nm). For MCS-s, owing to its wide bandgap (2.57 eV, Fig. 7c) and poor NIR light absorption (Fig. S12), MCS-s can not be excited to produce photo-generated electrons under NIR because the energy of NIR photons is lower than MCS-s's bandgap. As predicted, no H_2 production and no observable photo-current was detected from MCS-s under NIR (Fig. S11b), which also illustrates that MCS-s is hard to produce photo-induced electrons under NIR. In addition, pure Ni metal can not produce H_2 because Ni is photo-catalytically inactive for photocatalytic hydrogen evolution. Notably, a distinct photocurrent response can be observed for 1.5 wt% Ni/MCS-s (Fig. S11b) after Ni loading. The H_2 -production amount of 1.5 wt% Ni/MCS-s gradually increases with the illumination time. A possible schematic mechanism is shown in Fig. S13. Only plasmonic Ni can absorb the photons from NIR and generate "hot electrons" near the Fermi level of Ni. Then, a portion of "hot electrons" would transfer to the CB of MCS-s and participate in water reduction over MCS-s.

Fig. 5 shows the AQY values and cycling stability test. The AQY of 1.5 wt% Ni/MCS-s was 60.4% at 420 nm in 3.5 wt% NaCl (Fig. 5a), which is superior to those reported in previous studies on photocatalytic seawater splitting (Table S5). Besides, the trend of AQY values matches well with its optical absorption curve, meaning that this photocatalytic H_2 production reaction is driven by the absorption of incident photons

[45]. Cycle experiments (Fig. 5b) were followed to detect the substantial activity and stability of Ni/MCS-s under visible light irradiation. After four recycles, the activity of catalysts maintains stability. Furthermore, no obvious change was observed in the SEM images (Fig. S3c), XRD pattern (Fig. S14) and XPS spectra (Fig. S15) of the used sample, confirming the stability of the Ni/MCS-s composites in the photocatalytic process.

3.3. Photo-electrochemical properties and hydrophilicity analysis

The optical properties of Ni, MCS-s and Ni/MCS-s samples were analyzed by UV-vis diffuse reflectance spectroscopy (DRS). Pristine MCS-s has an intrinsic absorption edge at 510 nm (Fig. 6a). After Ni modifying, the Ni/MCS-s nanocomposites have a strong and broader absorption peak in the visible regime, which is attributed to the surface plasmon resonance of ultrathin Ni layer [18]. Photoluminescence (PL) and Time-resolved PL (TRPL) are powerful techniques to investigate charge carrier dynamics (Fig. 6b). At the excitation wavelength of 300 nm, the PL spectrum of pristine MCS-s presents a prominent emission peak at 533 nm, revealing the intense recombination of photo-induced carriers in MCS-s. It should be noted that the PL signal of 1.5 wt% Ni/MCS-s is remarkably quenched compared to that of MCS-s, indicating that the Ni layer helps to suppress the recombination of photo-carriers [46]. TRPL spectra (Fig. 6c) demonstrate that the average lifetime of charge carriers in 1.5 wt% Ni/MCS-s ($\tau = 0.704$ ns) is lower than that of MCS-s ($\tau = 0.971$ ns), which suggests the efficient interfacial electron transfer between MCS-s and Ni through Schottky contact [47].

A series of photoelectrochemical measurements were carried out to study the interfacial charge separation. In Fig. 6d, the photocurrent density is in the order of MCS-p < MCS-s < 1.0 wt% Pt/MCS-s < 1.5 wt% Ni/MCS-p < 1.5 wt% Ni/MCS-s, which reveals that the covering of Ni

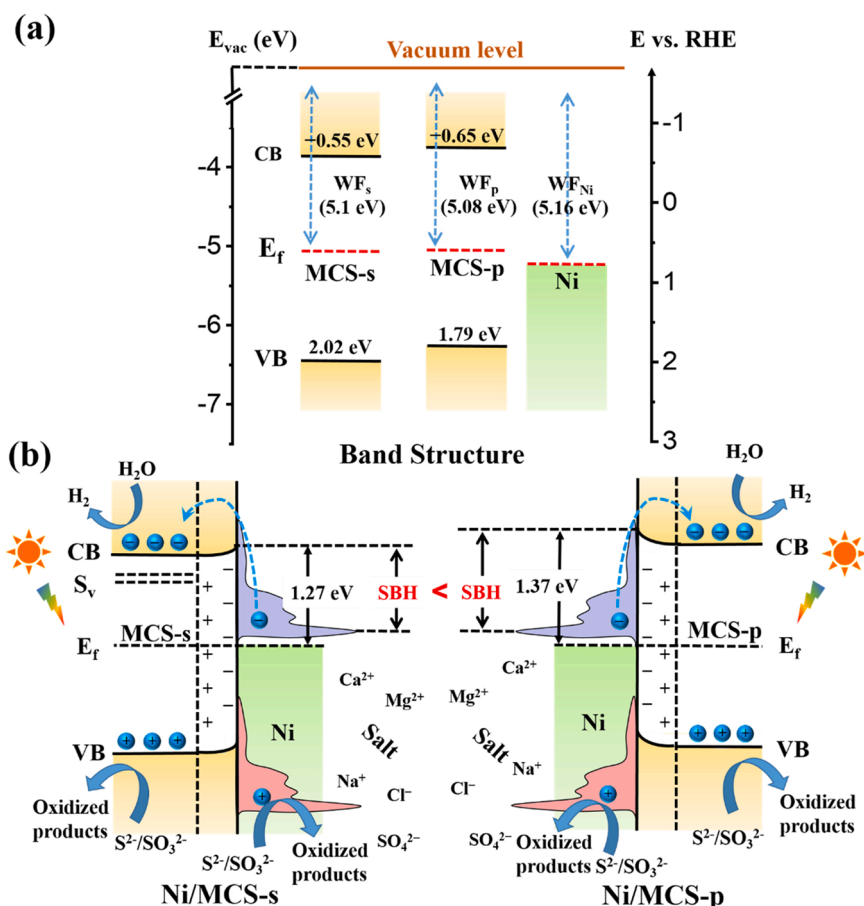


Fig. 8. (a) The band structure of MCS-s, MCS-p and Ni. (b) Schematic mechanism of H_2 production over Ni/MCS-s and Ni/MCS-p through photocatalytic reaction in seawater.

can efficiently boost the generation and migration of photo-carriers [48], even better than Pt modification. This result can also be proved by the electrochemical impedance spectroscopy (EIS) (Fig. 6e). 1.5 wt% Ni/MCS-s has the smallest semicircle, meaning that the Ni loading can effectively decrease the interfacial charge-transfer resistance. Besides, the semicircles of MCS-s and 1.5 wt% Ni/MCS-s become smaller when light on (Fig. S16), indicating the higher carrier density under light [49]. Fig. 6f presents the linear sweep voltammetry (LSV) measurements. The current density of the samples are in the order of MCS-p < MCS-s < 1.0 wt% Pt/MCS-s < 1.5 wt% Ni/MCS-p < 1.5 wt% Ni/MCS-s. This illustrates that the ultrathin Ni layer can reduce the overpotential, which is in favor of hydrogen production [35].

Hydrophilicity is a vital factor for the surface proton reduction reaction. Thus, we carried out water contact angle measurements over MCS-s and 1.5 wt% Ni/MCS-s (Fig. S17). The water contact angle (WCA) of Ni/MCS-s (19.2°) is smaller than that of MCS-s (33.1°), which demonstrates that the loading of the Ni layer could improve the hydrophilicity of MCS-s. Besides, the improvement in surface hydrophilicity provides more interaction sites with water, which is helpful for the improvement of H_2 evolution [50].

3.4. Possible mechanism of photocatalytic seawater splitting

To obtain insight into the charge transfer mechanism of Ni/MCS-s composite, Mott-Schottky plots, DRS and ultraviolet photoelectron spectroscopy (UPS) were performed to study the band structure. From the Mott-Schottky plots in Fig. 7a, the flat-band potential (V_{fb}) of MCS-s is -0.55 eV vs. RHE (-3.89 eV vs. vacuum). Considering that the difference between the V_{fb} and the bottom edge of the CB can be neglected

for n-type semiconductors [51], the V_{fb} is regarded as the conduction band position (E_{CB}) of MCS-s. Additionally, according to the Kubelka-Munk plot (Fig. 7c), the bandgap (E_g) of MCS-s is 2.57 eV. Combining the bandgap equation ($E_g = E_{VB} - E_{CB}$), the valence band position (E_{VB}) of MCS-s was calculated to be 2.02 eV vs. RHE (-6.46 eV vs. vacuum). Similarly, the E_{CB} , E_{VB} and E_g of MCS-p (Fig. 7b and Fig. 7d) is -0.65 eV vs. RHE (-3.79 eV vs. vacuum), 1.79 eV vs. RHE (-6.23 eV vs. vacuum), and 2.44 eV, respectively. Based on the definition of electron affinity (χ): the energy required to move an electron outside the semiconductor surface (i.e. vacuum level) from the bottom of the CB [52], the χ of MCS-s and MCS-p is 3.89 and 3.79 eV, respectively. Hence, the introduction of S vacancy leads to a lower χ for MCS-s. This is because S vacancy sites decrease the splitting between bonding and antibonding orbitals and thus increase electronic states within the bandgap of MCS-s [28]. The electronic states can induce the surface states and cause a down-shift in CB [30]. Moreover, according to the UPS results (Fig. S18a), the work function (WF_s) and Fermi level (E_f) of MCS-s were calculated to be 5.1 and -5.1 eV vs. vacuum, respectively, by subtracting the cutoff energy (16.12 eV) for secondary electrons from the He I excitation energy (21.22 eV). Similarly, the work functions for MCS-p (WF_p) and metallic nickel (WF_{Ni}) (Fig. S18b and Fig. S18c) were 5.08 eV and 5.16 eV, respectively. For comparison, the band structures of the samples are summarized in Fig. 8a.

Based on the above experimental results, a possible photocatalytic mechanism is proposed in Fig. 8. Given that WF_{Ni} is larger than WF_s (Fig. 8a), the electrons in MCS-s diffuse to Ni and the energy band of MCS-s bends upward to reach an equilibrium state of the Fermi level between MCS-s and Ni, which results in the formation of Schottky barriers. The presence of Schottky barriers hinders the electron flow over

the interface, especially from metal to semiconductor. However, S vacancies in MCS-s produce positive charge centers, increase the electronic states within the bandgap and form midgap defect states below the conduction band minimum [53] (Fig. 8b). These midgap defect states would serve as S vacancy levels (S_v) to trap electrons and hinder electrons diffusing to Ni when MCS-s is in intimate contact with Ni [54]. Meanwhile, the introduction of S vacancies induces surface states in the bandgap of MCS-s [28], which leads to the down-shift of the CB of MCS-s and thus decreases the SBH from 1.37 eV (MCS-p) to 1.27 eV (MCS-s). Under visible-light irradiation, the excitation of LSPR in the Ni layer transiently generates electron-hole pairs [17], some hot electrons can cross the Schottky barrier at the interface and inject into the CB of MCS-s for the reduction of H_2O to H_2 . Owing to the plasma oscillation, a fraction of hot electrons in plasmonic metals would distribute above the Fermi energy, which can further lower the SBH [27]. For instance, the hot electrons of Au center around the energy of about 0.7 eV above the Fermi energy under visible light, which can decrease its effective work function [27,55]. As a result, more plasmonic-induced electrons would transfer from Ni to the CB of MCS-s for the photocatalytic process. Furthermore, the Ni layer is helpful to hinder the corrosion of salts in seawater and keep the stability of catalysts. Due to the surface charge of the catalysts favoring the cation adsorption, the cations in seawater would promote the separation of plasmonic-induced electron-hole pairs from Ni, which attracts more electrons for boosting the photocatalytic reaction [7].

4. Conclusion

In summary, we have tuned the SBH of Ni/MCS-s heterostructures by coupling of plasmonic Ni and S vacancies for enhanced photocatalytic H_2 production in simulated seawater (3.5 wt% NaCl). The midgap defect states induced by S vacancies serve as an electron trap to restrain the recombination of photo-excited electron-hole pairs. Besides, the presence of S vacancies induces the surface states in the bandgap of MCS-s and leads to the down-shift of the CB of MCS-s, which decreases the SBH of Ni/MCS-s heterostructures. Moreover, the plasma oscillation of plasmonic Ni allows a fraction of hot electrons to distribute above the Fermi energy, thus further lowering the SBH between Ni and MCS-s. The decrease in SBH facilitates the migration of hot electrons from plasmonic Ni to MCS-s, which causes a higher H_2 -production yield for Ni/MCS-s. Furthermore, the Ni layer on the surface of MCS-s is helpful to hinder the corrosion of salts in seawater by adsorbing cations and would promote the separation of plasmonic-induced electron-hole pairs from Ni. As a consequence, the optimized Ni/MCS-s composite possesses excellent photocatalytic H_2 -production activity of up to 164.1 mmol/h/g in simulated seawater, which is higher than that in water (121.5 mmol/h/g), 68 times higher than that of pure MCS-s and approximately 5 times higher than that of 1 wt% Pt/MCS-s. Besides, the optimal AQY value reached 60.4% at 420 nm in simulated seawater, which is superior to those reported in previous studies on photocatalytic seawater splitting. This work highlights the synergistic effect of surface plasmon and intrinsic defects on the Schottky barrier for photocatalytic H_2 production, and provides a new idea for constructing metal-semiconductor photocatalysts.

CRedit authorship contribution statement

Chuchu Cheng prepared the manuscript. Chuchu Cheng and Jingwen Zhang contributed to the data collection and analysis. Fangshu Xing and Renyou Zeng help to analyze the characterization experiment data. Caijin Huang conceived the project and supervised the research.

Declaration of Competing Interest

The authors declare that they have no known competing financial

interests or personal relationships that could have appeared to influence the work reported in this paper.

Acknowledgments

This work was supported by the National Natural Science Foundation of China (grant nos. 22072024 and U1662112).

Appendix A. Supporting information

Supplementary data associated with this article can be found in the online version at doi:10.1016/j.apcatb.2022.121321.

References

- [1] M.C. Liu, Y.B. Chen, J.Z. Su, J.W. Shi, X.X. Wang, L.J. Guo, Photocatalytic hydrogen production using twinned nanocrystals and an unanchored NiS_x co-catalyst, *Nature Energy* 1 (2016) 16151.
- [2] H. Wang, X. Li, X. Zhao, C. Li, X. Song, P. Zhang, P. Huo, X. Li, A review on heterogeneous photocatalysis for environmental remediation: from semiconductors to modification strategies, *Chin. J. Catal.* 43 (2022) 178–214.
- [3] J. Rozema, T. Flowers, Crops for a salinized world, *Science* 322 (2008) 1478–1480.
- [4] J.N. Zhang, W.P. Hu, S. Cao, L.Y. Piao, Recent progress for hydrogen production by photocatalytic natural or simulated seawater splitting, *Nano, Research* 13 (2020) 2313–2322.
- [5] S.M. Ji, H. Jun, J.S. Jang, H.C. Son, P.H. Borse, J.S. Lee, Photocatalytic hydrogen production from natural seawater, *J. Photochem. Photobiol., A* 189 (2007) 141–144.
- [6] Y.X. Li, F. He, S.Q. Peng, D. Gao, G.X. Lu, S.B. Li, Effects of electrolyte NaCl on photocatalytic hydrogen evolution in the presence of electron donors over Pt/TiO₂, *J. Mol. Catal. A: Chem.* 341 (2011) 71–76.
- [7] Q.Y. Wu, J.J. Cao, X. Wang, Y. Liu, Y.J. Zhao, H. Wang, Y. Liu, H. Huang, F. Liao, M.W. Shao, Z.H. Kang, A metal-free photocatalyst for highly efficient hydrogen peroxide photoproduction in real seawater, *Nat. Commun.* 12 (2021) 483.
- [8] M. Gao, P.K.N. Connor, G.W. Ho, Plasmonic photothermal directed broadband sunlight harnessing for seawater catalysis and desalination, *Energy Environ. Sci.* 9 (2016) 3151–3160.
- [9] X.Y. Yang, Z.C. Hu, Q.W. Yin, C. Shu, X.F. Jiang, J. Zhang, X.H. Wang, J.X. Jiang, F. Huang, Y. Cao, Water-soluble conjugated molecule for solar-driven hydrogen evolution from salt water, *Adv. Funct. Mater.* 29 (2019), 1808156.
- [10] A.J. Simamora, T.L. Hsiung, F.C. Chang, T.C. Yang, C.Y. Liao, H.P. Wang, Photocatalytic splitting of seawater and degradation of methylene blue on CuO/nano TiO₂, *Int. J. Hydrog. Energy* 37 (2012) 13855–13858.
- [11] B.C. Qiu, Q.H. Zhu, M.Y. Xing, J.L. Zhang, A robust and efficient catalyst of $Cd_xZn_{1-x}Se$ motivated by CoP for photocatalytic hydrogen evolution under sunlight irradiation, *Chem. Commun.* 53 (2017) 897–900.
- [12] W.M. Xu, X.D. Zhao, X.H. An, S. Wang, J. Zhang, Z.S. Li, W.T. Wu, M.B. Wu, Alkali halide boost of carbon nitride for photocatalytic H_2 evolution in seawater, *ACS Appl. Mater. Interfaces* 12 (2020) 48526–48532.
- [13] W. Wu, X.Q. Cheng, J.B. Zhao, X.G. Li, Benefit of the corrosion product film formed on a new weathering steel containing 3% nickel under marine atmosphere in Maldives, *Corros. Sci.* 165 (2020), 108416.
- [14] Z.L. Wang, J.J. Fan, B. Cheng, J.G. Yu, J.S. Xu, Nickel-based cocatalysts for photocatalysis: hydrogen evolution, overall water splitting and CO₂ reduction, *Mater. Today Phys.* 15 (2020), 100279.
- [15] R. Shen, K. He, A. Zhang, N. Li, Y.H. Ng, P. Zhang, J. Hu, X. Li, In-situ construction of metallic $Ni_3C@Ni$ core-shell cocatalysts over g-C₃N₄ nanosheets for shell-thickness-dependent photocatalytic H_2 production, *Appl. Catal., B* 291 (2021), 120104.
- [16] C. Bhattacharya, S.E. Saji, A. Mohan, V. Madav, G.H. Jia, Z.Y. Yin, Sustainable nanoplasmon-enhanced photoredox reactions: synthesis, characterization, and applications, *Adv. Energy Mater.* 10 (2020), 2002402.
- [17] S. He, J.W. Huang, J.L. Goodsell, A. Angerhofer, W.D. Wei, Plasmonic nickel-TiO₂ heterostructures for visible-light-driven photochemical reactions, *Angew. Chem., Int. Ed.* 58 (2019) 6038–6041.
- [18] L. Pei, T.Z. Li, Y.J. Yuan, T. Yang, J.S. Zhong, Z.G. Ji, S.C. Yan, Z.G. Zou, Schottky junction effect enhanced plasmonic photocatalysis by TaON@Ni NP heterostructures, *Chem. Commun.* 55 (2019) 11754–11757.
- [19] C.Y. Zhang, F.C. Jia, Z.Y. Li, X. Huang, G. Lu, Plasmon-generated hot holes for chemical reactions, *Nano. Res.* 13 (2020) 3183–3197.
- [20] S. Yu, Y.H. Kim, S.Y. Lee, H.D. Song, J. Yi, Hot-electron-transfer enhancement for the efficient energy conversion of visible light, *Angew. Chem., Int. Ed.* 53 (2014) 11203–11207.
- [21] R. Shen, D. Ren, Y. Ding, Y. Guan, Y.H. Ng, P. Zhang, X. Li, Nanostructured CdS for efficient photocatalytic H_2 evolution: a review, *Sci. China Mater.* 63 (2020) 2153–2188.
- [22] X.Y. Shi, S. Posyasaev, M. Huttula, V. Pankratov, J. Hozzowska, J.C. Dousse, F. Zeeshan, Y.R. Niu, A. Zakharov, T.H. Li, O. Miroshnichenko, M. Zhang, X. Wang, Z.J. Huang, S. Saukko, D.L. Gonzalez, S. van Dijken, M. Alatalo, W. Cao, Metallic contact between MoS₂ and Ni via Au nanoglue, *Small* 14 (2018), 1704526.
- [23] A. Wang, S.J. Wu, J.L. Dong, R.X. Wang, J.W. Wang, J.L. Zhang, S.X. Zhong, S. Bai, Interfacial facet engineering on the Schottky barrier between plasmonic Au and

- TiO₂ in boosting the photocatalytic CO₂ reduction under ultraviolet and visible light irradiation, *Chem. Eng. J.* 404 (2021), 127145.
- [24] H.Y. Bai, S.H. Lam, J.H. Yang, X.Z. Cheng, S.S. Li, R.B. Jiang, L. Shao, J.F. Wang, A Schottky-barrier-free plasmonic semiconductor photocatalyst for nitrogen fixation in a "one-stone-two-birds" manner, *Adv. Mater.* (2021), 2104226.
- [25] H. Li, J. Shang, Z.H. Ai, L.Z. Zhang, Efficient visible light nitrogen fixation with BiOBr nanosheets of oxygen vacancies on the exposed {001} facets, *J. Am. Chem. Soc.* 137 (2015) 6393–6399.
- [26] P. Jimenez-Calvo, V. Caps, V. Keller, Plasmonic Au-based junctions onto TiO₂, gC₃N₄, and TiO₂-gC₃N₄ systems for photocatalytic hydrogen production: fundamentals and challenges, *Renew. Sustain. Energy Rev.* 149 (2021), 111095.
- [27] B.F. Zhao, I. Aravind, S.S. Yang, Y. Wang, R.X. Li, B.X. Zhang, Y. Wang, J. M. Dawlaty, S.B. Cronin, Enhanced plasma generation from metal nanostructures via photoexcited hot electrons, *J. Phys. Chem. C* 125 (2021) 6800–6804.
- [28] S. Bai, N. Zhang, C. Gao, Y.J. Xiong, Defect engineering in photocatalytic materials, *Nano Energy* 53 (2018) 296–336.
- [29] I. Marri, S. Ossicini, Oxygen vacancy effects on the Schottky barrier height at the Au/TiO₂(110) interface: a first principle study, *Solid State Commun.* 147 (2008) 205–207.
- [30] H.L. Guo, Z.F. Zhang, Y.Z. Guo, Z.B. Gao, R.S. Zheng, H.L. Wu, Impact of the interface vacancy on Schottky barrier height for Au/AlN polar interfaces, *Appl. Surf. Sci.* 505 (2020), 144650.
- [31] X. Li, Y.Z. Xia, J.F. Hou, W. Lin, T. Chen, Y.P. Wu, Z.M. Wu, J.Y. Kang, Engineering sulfur vacancies in WS₂/Au interface toward ohmic contact, *Appl. Phys. A: Mater. Sci. Process.* 127 (2021) 644.
- [32] X.R. Gan, D.Y. Lei, K.Y. Wong, Two-dimensional layered nanomaterials for visible-light-driven photocatalytic water splitting, *Mater. Today, Energy* 10 (2018) 352–367.
- [33] X. Wang, X. Wang, J. Huang, S. Li, A. Meng, Z. Li, Interfacial chemical bond and internal electric field modulated Z-scheme S_v-ZnIn₂S₄/MoSe₂ photocatalyst for efficient hydrogen evolution, *Nat. Commun.* 12 (2021) 4112.
- [34] C.C. Cheng, J.N. Wang, X.S. Guo, F.S. Xing, C.J. Huang, M.X. Song, Thermal-assisted photocatalytic H₂ production over sulfur vacancy-rich Co_{0.85}Se/Mn_{0.3}Cd_{0.7}S nanorods under visible light, *Appl. Surf. Sci.* 557 (2021), 149812.
- [35] J.W. Zhang, C.C. Cheng, F.S. Xing, C. Chen, C.J. Huang, 0D β-Ni(OH)₂ nanoparticles/1D Mn_{0.3}Cd_{0.7}S nanorods with rich S vacancies for improved photocatalytic H₂ production, *Chem. Eng. J.* 414 (2021), 129157.
- [36] D. Gao, X. Wu, P. Wang, H. Yu, B. Zhu, J. Fan, J. Yu, Selenium-enriched amorphous NiSe_{1-x} nanoclusters as a highly efficient cocatalyst for photocatalytic H₂ evolution, *Chem. Eng. J.* 408 (2020), 127230.
- [37] X.X. Lu, W.J. Chen, Y. Yao, X.M. Wen, J.N. Hart, C. Tsounis, C.Y. Toe, J. Scott, Y. H. Ng, Photogenerated charge dynamics of CdS nanorods with spatially distributed MoS₂ for photocatalytic hydrogen generation, *Chem. Eng. J.* 420 (2021), 127709.
- [38] K.V. Manukyan, A.V. Yeghishyan, V. Danghyan, S. Rouvimov, A.S. Mukasyan, E. E. Wolf, Structural transformations of highly porous nickel catalysts during ethanol conversion towards hydrogen, *Int. J. Hydrog. Energy* 43 (2018) 13225–13236.
- [39] H.S. Gong, Q.W. Liu, C.J. Huang, NiSe as an effective co-catalyst coupled with TiO₂ for enhanced photocatalytic hydrogen evolution, *Int. J. Hydrog. Energy* 44 (2019) 4821–4831.
- [40] V.K. Sharma, A. Baiker, Superparamagnetic effects in the ferromagnetic resonance of silica supported nickel particles, *J. Chem. Phys.* 75 (1981) 5596–5601.
- [41] S.C. Xu, E.D. Walter, Z.C. Zhao, M.Y. Hu, X.W. Han, J.Z. Hu, X.H. Bao, Dynamic structural changes of SiO₂ supported Pt-Ni bimetallic catalysts over redox treatments revealed by NMR and EPR, *J. Phys. Chem. C* 119 (2015) 21219–21226.
- [42] J.W. Pan, G.X. Zhang, Z.J. Guan, Q.Y. Zhao, G.Q. Li, J.J. Yang, Q.Y. Li, Z.G. Zou, Anchoring Ni single atoms on sulfur-vacancy-enriched ZnIn₂S₄ nanosheets for boosting photocatalytic hydrogen evolution, *J. Energy Chem.* 58 (2021) 408–414.
- [43] Q.-Z. Huang, Z.-J. Tao, L.-Q. Ye, H.-C. Yao, Z.-J. Li, Mn_{0.2}Cd_{0.8}S nanowires modified by CoP₃ nanoparticles for highly efficient photocatalytic H₂ evolution under visible light irradiation, *Appl. Catal., B* 237 (2018) 689–698.
- [44] B. Wang, S. He, L.L. Zhang, X.Y. Huang, F. Gao, W.H. Feng, P. Liu, CdS nanorods decorated with inexpensive NiCd bimetallic nanoparticles as efficient photocatalysts for visible-light-driven photocatalytic hydrogen evolution, *Appl. Catal., B* 243 (2019) 229–235.
- [45] B. Tian, Y. Wu, G. Lu, Metal-free plasmonic boron phosphide/graphitic carbon nitride with core-shell structure photocatalysts for overall water splitting, *Appl. Catal., B* 243 (2021), 119410.
- [46] G.G. Zhang, G.S. Li, Z.A. Lan, L.H. Lin, A. Savateev, T. Heil, S. Zafeirotas, X. C. Wang, M. Antonietti, Optimizing optical absorption, exciton dissociation, and charge transfer of a polymeric carbon nitride with ultrahigh solar hydrogen production activity, *Angew. Chem., Int. Ed.* 56 (2017) 13445–13449.
- [47] X.J. Wang, X. Tian, Y.J. Sun, J.Y. Zhu, F.T. Li, H.Y. Mu, J. Zhao, Enhanced Schottky effect of a 2D–2D CoP/g-C₃N₄ interface for boosting photocatalytic H₂ evolution, *Nanoscale* 10 (2018) 12315–12321.
- [48] C.X. Xu, S.H. Wu, G.P. Xiong, X.Z. Guo, H.C. Yang, J.H. Yan, K.F. Cen, Z. Bo, K. Ostrikov, Nanoconfined fusion of g-C₃N₄ within edge-rich vertically oriented graphene hierarchical networks for high-performance photocatalytic hydrogen evolution utilizing superhydrophilic and superaerophobic responses in seawater, *Appl. Catal., B* 280 (2021), 119461.
- [49] B.T. Sun, P.Y. Qiu, Z.Q. Liang, Y.J. Xue, X.L. Zhang, L. Yang, H.Z. Cui, J. Tian, The fabrication of 1D/2D CdS nanorod@Ti₃C₂ MXene composites for good photocatalytic activity of hydrogen generation and ammonia synthesis, *Chem. Eng. J.* 406 (2021).
- [50] Q. Zhang, X. Bai, X. Hu, J. Fan, E. Liu, Efficient photocatalytic H₂ evolution over 2D/2D S-scheme NiTe₂/g-C₃N₄ heterojunction with superhydrophilic surface, *Appl. Surf. Sci.* 579 (2022), 152224.
- [51] S.J. Hong, S. Lee, J.S. Jang, J.S. Lee, Heterojunction BiVO₄/WO₃ electrodes for enhanced photoactivity of water oxidation, *Energy Environ. Sci.* 4 (2011) 1781–1787.
- [52] M. Mishra, S. Krishna, N. Aggarwal, G. Gupta, Influence of metallic surface states on electron affinity of epitaxial AlN films, *Appl. Surf. Sci.* 407 (2017) 255–259.
- [53] Y.Y. Qin, H. Li, J. Lu, Y.H. Feng, F.Y. Meng, C.C. Ma, Y.S. Yan, M.J. Meng, Synergy between van der Waals heterojunction and vacancy in ZnIn₂S₄/g-C₃N₄ 2D/2D photocatalysts for enhanced photocatalytic hydrogen evolution, *Appl. Catal., B* 277 (2020), 119254.
- [54] X. Li, Y. Cheng, Q.P. Wu, J. Xu, Y.S. Wang, Synergistic effect of the rearranged sulfur vacancies and sulfur interstitials for 13-fold enhanced photocatalytic H₂ production over defective Zn₂In₂S₅ nanosheets, *Appl. Catal., B* 240 (2019) 270–276.
- [55] S.Y. Moon, H.C. Song, E.H. Gwag, I.I. Nedrygailov, C. Lee, J.J. Kim, W.H. Doh, J. Y. Park, Plasmonic hot carrier-driven oxygen evolution reaction on Au nanoparticles/TiO₂ nanotube arrays, *Nanoscale* 10 (2018) 22180–22188.